

Multimodal End-to-End Autonomous Driving

Yi Xiao, Felipe Codevilla, Akhil Gurram, Onay Urfalioglu, Antonio M. López

Abstract—Autonomous vehicles (AVs) are key for the intelligent mobility of the future. A crucial component of an AV is the artificial intelligence (AI) able to drive towards a desired destination. Today, there are different paradigms addressing the development of AI drivers. On the one hand, we find modular pipelines, which divide the driving task into sub-tasks such as perception (*e.g.* object detection, semantic segmentation, depth estimation, tracking) and maneuver control (*e.g.* local path planning and control). On the other hand, we find end-to-end driving approaches that try to learn a direct mapping from input raw sensor data to vehicle control signals (*e.g.* the steering angle). The later are relatively less studied, but are gaining popularity since they are less demanding in terms of sensor data annotation. This paper focuses on end-to-end autonomous driving. So far, most proposals relying on this paradigm assume RGB images as input sensor data. However, AVs will not be equipped only with cameras, but also with active sensors providing accurate depth information (*e.g.*, traditional LiDARs, or new solid state ones). Accordingly, this paper analyses if RGB and depth data, *i.e.* RGBD data, can actually act as complementary information in a multimodal end-to-end driving approach, producing a better AI driver. Using the CARLA simulator functionalities, its standard benchmark, and conditional imitation learning (CIL), we will show how, indeed, RGBD gives rise to more successful end-to-end AI drivers. We will compare the use of RGBD information by means of early, mid and late fusion schemes, both in multisensory and single-sensor (monocular depth estimation) settings.

Index Terms—Multimodal scene understanding, End-to-end autonomous driving, Imitation learning.

I. INTRODUCTION

HERE is increasing consensus about the need of progressively moving towards new models of mobility as a service, aiming at (1) reducing traffic accidents, congestion and pollution; (2) improving the mobility of temporally or permanent handicapped people, as well as the elderly; (3) achieving time efficiency when delivering goods and transporting persons. Autonomous vehicles (AVs) are core for such new paradigms of mobility. Developing AVs is a tremendous multidisciplinary challenge involving topics such as route planning, environment perception, maneuver control, vehicle-to-X cooperation, cyber-security; all governed by ethical and legal aspects. Focusing on the scientific-technical topics, one of the essential challenges today is how to develop the artificial intelligence (AI) that would allow vehicles to drive autonomously.

Yi Xiao, Felipe Codevilla, and Antonio M. López are with the Computer Vision Center (CVC) and the Univ. Autònoma de Barcelona (UAB). Akhil Gurram is with the CVC/UAB and Huawei GRC in Munich. Onay Urfalioglu is with Huawei GRC in Munich.

We acknowledge the financial support by the Spanish TIN2017-88709-R (MINECO/AEI/FEDER, UE). Antonio M. López acknowledges the financial support by ICREA under the ICREA Academia Program. Felipe Codevilla acknowledges Catalan AGAUR for his FI grant 2017FI-B1-00162. Yi Xiao acknowledges the Chinese Scholarship Council (CSC), grant number 201808390010. We also thank the Generalitat de Catalunya CERCA Program, as well as its ACCIO agency.

Accordingly, the research community is currently exploring different paradigms for developing AI drivers, from modular pipelines to end-to-end driving models.

The modular paradigm attaches to the traditional divide-and-conquer engineering principle, since AI drivers rely on clearly defined modules with particular responsibilities; for instance, to provide environmental perception [1], [2], as well as route planning and maneuver control [3], [4]. Just environmental perception is already specially complex, since we can find a plethora of associated sub-tasks such as object detection (2D image-based [5], [6], [7], 3D image-based [8], [9], 3D LiDAR-based [10], [11], [12], [13], [14], [15], and multimodal [16], [17], [18], [19], [20], [21], [22], [23]); object tracking (image-based [24], [25], [26], [27], [28], [29], [30], multimodal [31]); traffic sign recognition [32]; semantic segmentation (by class/category [33], [34], [35] and object instances [36], [37], [38], usually based on images of the visual spectrum but also on multimodal data [39], [40]); monocular depth estimation [41], [42], [43], [44]; stixel-world representation (based on stereo images [45], [46], [47], [48], monocular [49], [50], and multimodal [51]); as well as SLAM and place recognition [52], [53], [54], [55], [56], [57], [58], [59], [60], [61].

The end-to-end paradigm is closer to both human nature and pure AI, since it aims at developing holistic sensorimotor driving models [62], [63], [64], [65]. Thus, on the one hand, the end-to-end paradigm is similar to human nature since we do not learn to perceive the world and acting on it as separate tasks, we learn to perceive and act simultaneously; on the other hand, these driving models are developed by a pure data-driven supervised learning process as is characteristic of AI. Sometimes pure end-to-end models are modified for solving intermediate sub-tasks such as predicting affordances [66], [67] or waypoints [68], [69], for accepting high-level navigation commands [70], [71], [72], [73], or restricted to very specific navigation sub-tasks such as lane keeping [74], [75], [76] and longitudinal control [77].

Nowadays, modular and end-to-end driving paradigms are highly relying on convolutional neural networks (CNNs). In this context, one of the main advantages of modular pipelines is the ability to explain the decisions of the AI driver in terms of its modules; which is more difficult for pure end-to-end driving models [78], [79], [80]. However, some of the critical modules involved in the modular paradigm have the problem of requiring hundreds of thousands of supervised data samples [81], [82], *e.g.* raw sensor data with ground truth (GT). Since the GT is most of the times provided manually (*e.g.* annotation of object bounding boxes [83], pixel-level delineation of semantic classes [84]), this is an important bottleneck for the modular paradigm. Conversely, pure end-to-end approaches are able to learn CNN-based models for driving from raw sensor data (*i.e.* without annotated GT) and

associated supervision in terms of vehicle's variables (*e.g.* steering angle, speed, geo-localization and orientation [85], [86], [65]); note that such supervision does not require human intervention in terms of explicitly annotating the content of the raw sensor data. Moreover, end-to-end models are demonstrating an *unreasonable* effectiveness in practice [64], [75], [71], [77] which makes worth to go deeper in their study.

There are two main approaches in the end-to-end driving paradigm, namely reinforcement learning [87], [88], [89] and imitation learning [90], [91]. The former approach usually requires millions of trial-and-error driving episodes which, in the case of AV development, is not affordable on real roads since initial learning episodes would have an enormous risk of ending in an accident. The latter approach¹ has not this problem since it consists of accumulating hundred of hours of human driving in the form of datasets (expert demonstrations), and then performing an offline data-driven learning as a sort of driving cloning but without the intervention of human drivers (experts). Therefore, only in testing time, *i.e.* after a comprehensive training process, the corresponding AVs need to actually operate autonomously in the real world. In fact, reinforcement learning cycles can be considered after a solid imitation learning process [73].

Although AVs will be multisensory platforms, equipping and maintaining on-board synchronized heterogeneous sensors is quite expensive nowadays. As a consequence, most of the end-to-end models for driving by imitation rely only on vision [62], [63], [66], [64], [65], [74], [75], [76], [71], [67], [68], [69], [93], [72], [73], [77], *i.e.* they are visuomotor models. This is not bad in itself, after all, human drivers mainly rely on vision and these models aim at imitate them. However, multimodality has shown better performance in key perception sub-tasks such as object detection [94], [17], [18], [14], [19], [20], [21], [22], [23], tracking [31], semantic segmentation [39], [40], and stixel-world representation [51]. Therefore, it is worth to explore multimodality in the context of end-to-end driving models. However, the literature on this topic is still scarce [95], [96]. In fact, a survey paper on multimodal object detection and semantic segmentation, appeared during the elaboration of this paper, states that *multimodal end-to-end learning and direct perception* (which refers to what we term here as *multimodal end-to-end driving*) is still an open question (see [97], C.2).

Accordingly, in this paper we address the question *can an end-to-end model, learned by driver imitation, actually drive better using multimodal sensor data than just relying on a single modality?* In particular, as is common in modular pipelines, as single modalities we assume color images (RGB) and depth (D), and RGBD as multimodal data. Due to its capability of accepting high level commands, this study will be based on the CNN architecture known as conditional imitation learning (CIL) [71]. We explore RGBD from the perspective of early, mid and late fusion of the RGB and D modalities. In

¹It is worth to note that using the term *imitation learning* can be controversial, since the technical approaches used for end-to-end driving would be called *learning by demonstration* by some authors in the general field of robotics [92]. However, we keep using the term *imitation learning* here as currently is the most common in end-to-end driving literature.

early fusion, the raw RGB and D data are fused at the input of the CIL architecture; in mid fusion, intermediate CIL feature layers from RGB and D streams are fused; in late fusion, the output (maneuver commands) of the RGB and D CIL architecture are fused. Note that late and mid fusion require more computation power than early fusion since, roughly speaking, the CIL CNN is duplicated.

In order to answer the posed question, as is being common practice in many recent previous works on end-to-end driving [71], [68], [67], [69], [72], [73], [80], we will rely on the open source driving simulator known as CARLA [98] and its standard benchmark.

The presented results will show how, indeed, the multimodal RGBD end-to-end driving models outperform their single-modal counterparts; also, being on par or outperforming other state-of-the-art end-to-end approaches that introduce sub-tasks such as estimation of affordances. In fact, we will see that the best fusion approach in terms of driving and computational efficiency is early fusion, therefore, this use of RGBD information is totally complementary and compatible with other literature approaches to end-to-end driving (based on the estimation of affordances, waypoints, etc.). On the other hand, monocular image-based RGBD input does not outperforms multisensory RGBD; however, we will see how this special case of single-sensor multimodal end-to-end models, or visuomotor multimodal models, still are worth to be pursued in the future.

We detail all this work as follows. In Sect. II, we summarize the most related literature to ours. Sect. III presents the used CIL architecture from the point of view of early, mid, and late fusion. In Sect. IV, we summarize the training dataset and driving benchmark used to perform the different experiments, the obtained results and its corresponding quantitative and qualitative analysis. Finally, Sect. V draws the main conclusions and future work.

II. RELATED WORK

Once contextualized our work, it is clear that the two more related topics are multimodal perception and end-to-end driving models learned by imitation, thus, this section focuses on both.

Due to its inherent difficulty, object detection has been one of the tasks of the environmental perception pipeline for which multimodality has received more attention so far. Enzweiler *et al.* [16] developed a pedestrian detector using hand-crafted features and shallow classifiers combined in the form of a mixture-of-experts strong classifier, where the multimodality mainly arises after using image intensity and depth from stereo as raw sensor data. Gonzalez *et al.* [17] also addressed the detection of vehicles, pedestrians and cyclists (*i.e.* VRUs—vulnerable road users—), following such a mixture-of-experts paradigm, where multimodality relies on input sensor data in the form of calibrated (*i.e.* registered in space and synchronized in time) RGB and dense depth from LiDAR images. Chen *et al.* [18] also use calibrated RGB and depth from LiDAR images as input to a CNN-based object detector for vehicles and VRUs. The approach relying on CNNs to detect

vehicles and/or VRUs from RGB and depth from LiDAR images is a current trend, as can be seen in Asvadi *et al.* [19], where YOLO [7] is used as core CNN architecture, Pfeuffer *et al.* [21] who rely on VGG16 [99] (as done by Chen *et al.* [18]), as well as Ku *et al.* [20] and Wu *et al.* [23], who use customized CNNs. Focusing on CNN-based works, which are providing top-best results in public benchmarks such as KITTI dataset [83], we can see that some approaches are inspired by the Faster R-CNN architecture [5] because they consists of a first stage aiming at proposing candidate regions to contain objects of interest, and a second stage performing the classification of those regions to provide final object detections; *i.e.* following a mid-level (deep) fusion scheme where CNN layers of features from the different modalities are fused in both stages [18], [20], [23]. Alternative approaches are the early fusion at the raw data level [21], as well as the late fusion of the output of independent detectors [19], [21]. It is also worth to note that there are approaches which, rather than performing what can be considered as modality fusion, use the different modalities at separated steps of the object detection pipeline. For instance, Qi *et al.* [14] use RGB and calibrated LiDAR data, but in this case the RGB image is used to generate 2D candidate bounding boxes which define a 3D view frustum in the LiDAR point cloud, where object detection is finally performed solely using the LiDAR data.

The works mentioned so far focus on the use of RGBD data, *i.e.* they combine appearance (from RGB, and partially from the luminance channel of LiDAR) and geometry (from Depth, either based on LiDAR or stereo rigs) to robustify object detection. We can find also approaches that focus on multispectral appearance as the basis to develop more robust object detectors. For instance, Li *et al.* [14] compare different fusion schemes using Faster R-CNN as core CNN architecture to process RGB and Far Infrared (FIR) calibrated images. Eventually, such detectors should be more robust to adverse illumination conditions (*e.g.* nighttime). In fact, fusing RGB, FIR and LiDAR can become an interesting topic to explore.

What is common to all these studies is that, indeed, object detection accuracy increases with multimodality. For more details on multimodal object detection, the reader is referred to recent surveys [100], [97].

Due to the success of multimodality in object detection, more perception tasks have been addressed under the multimodal approach. Dimitrievski *et al.* [31] propose a pedestrian tracker that fuses camera and LiDAR detections to solve the data association step of their tracking-by-detection approach. Schneider *et al.* [39] propose a CNN architecture for semantic segmentation which performs a mid-level fusion of RGB and depth-from-stereo data, leading to a more accurate segmentation on small objects. Ha *et al.* [40] also propose a mid-level fusion approach in CNN architecture for semantic segmentation, however, in this case the multimodality is provided by calibrated RGB and FIR images. Piewak *et al.* [51] use a mid-level fusion of LiDAR and camera data to produce a Stixel representation of the driving scene, showing improved accuracy in terms of geometry and semantics of the resulting representation.

In this paper, rather than focusing on individual perception

tasks such as object detection, tracking or semantic segmentation, we challenge multimodality in the context of end-to-end driving, exploring early, mid and late fusion schemes.

Pomerleau [62] presented ALVINN three decades ago, a sensorimotor fully-connected shallow neural network able to perform road following assuming no obstacles, which is the first evidence of end-to-end driving. ALVINN was driving at $\sim 2\text{Km/h}$ the CMU's Chevy van called NAVLAB for 400m in a straight path under good weather conditions. Interestingly, although the addressed scenario is extremely simple compared to driving in real traffic, it was already necessary simulating data to train the sensorimotor model and, in fact, camera images (30×32 pixels, blue channel) were already combined by early fusion with laser range finder data (8×32 depth cells). Even the necessity to teach the network on recovering from errors was already pointed out in this pioneering work, a common practice today when training end-to-end driving models. Another pioneering work on end-to-end driving was presented by LeCun *et al.* [63]. In this case, a 6-layer CNN is trained end-to-end for off-road obstacle avoidance using image pairs as input (the cameras were located as in a stereo rig configuration). Such CNN was able to control a 50cm-length four-wheel truck, DAVE, for moving avoiding obstacles at a speed of $\sim 7\text{Km/h}$. During data collection for training, the truck was remotely controlled by a human operator, thus, the CNN was trained according to imitation learning in our terminology (or teleoperation-based demonstration according to [92]). More recently, Bojarski *et al.* [64] developed a vision-based end-to-end driving CNN able to control the steering wheel of a real car in different traffic conditions. Such CNN consists of a considerably larger number of parameters than ALVINN and DAVE's CNN, namely $\sim 250\text{K}$. The capabilities of this CNN exclude lane and road changing; moreover, since throttle and brake are not controlled it is not able to perform automatic stop-and-go maneuvers. During CNN training, recovering from steering errors is ingeniously simulated to obtain a more robust model.

These pioneering works have inspired new proposals within the imitation learning paradigm based on CNN architectures. Eraqi *et al.* [76] applied vision-based end-to-end control of the steering angle (neither throttle nor break), focusing on including temporal reasoning by means of long short-term memory recurrent neural networks (LSTMs). Training and testing were done in the Comma.ai dataset [85]. George *et al.* [77] applied similar ideas for controlling the speed of the car. Xu *et al.* [65] focused on vision-based prediction of the steering angle using a fully convolutional network (FCN) and a LSTM, in this case, forcing semantic segmentation as an auxiliary task during training. Training and testing were done in the BDDV dataset presented as part of the same work. Innocenti *et al.* [74] performed vision-based end-to-end steering angle prediction for lane keeping on private datasets. Similarly, Chen *et al.* [75] perform lane keeping by steering angle prediction in the Comma.ai dataset.

Using datasets to develop end-to-end AI drivers, has the problem of evaluating driving performance in a static world, where only steering angle use to be predicted. Moreover, defining evaluation metrics for static datasets that correlate

well with actual driving performance is not straightforward [101]. Accordingly, there are many works that rely on driving simulators, as is the case in the following works.

Chen *et al.* [66] and Sauer *et al.* [67] have explored the use of affordances (*e.g.* *Red Traffic Light*, *Distance to preceding vehicle*, etc.) as intermediate tasks between perception and prediction of the vehicle control parameters. Note that such affordances do not require to solve perception sub-task such as explicit object detection, etc; the underlying idea is to rely on a set of compact but complete description of the factors that influence driving according to prior human knowledge. Chen *et al.* trained and tested their model using the TORCS simulator [102], so in car racing conditions (no pedestrians, no intersections, etc.) under clean and dry weather, while Sauer *et al.* used the CARLA simulator which supports regular traffic conditions under different lighting and weathers [98]. Muller *et al.* [68] developed a vision-based CNN architecture with an intermediate road segmentation task for learning to perform vehicle maneuvers in a semantic space; in particular, the driving policy consists of predicting waypoints within the segmented road and applying a low-level PID controller afterwards. Training and testing is done in CARLA, but neither incorporating other vehicles nor pedestrians. Rhinehart *et al.* [69] combined imitation learning and model-based reinforcement learning to develop probabilistic models able to predict expert-like vehicle trajectories, in this case relying on LiDAR data, also using CARLA to elaborate their proposal but without including other vehicles and pedestrians.

Conventional end-to-end driving models are not explicitly designed to accept high-level navigation instructions such as *turn left in the next intersection* (without providing explicit distance information), which can come from a global planner or just as voice commands from a passenger of the AV. Hubschneider *et al.* [70] proposed to feed a turn indicator in the vision-based CNN driving model by concatenating it with features of a mid-level fully connected layer of the CNN. Codevilla *et al.* [71] addressed the same problem by a different method that turned out to be more effective. In particular, it is proposed a vision-based CNN consisting of a initial block agnostic to particular navigation instructions, and a second block branched according to a subset of navigation instructions (*viz.* at next intersection turn-left/turn-right/go-straight, or just continue current direction). In the first block, vehicle information is also incorporated as mid-level feature of the CNN; in particular, current speed is used since the CNN controls the steering angle, the throttle, and the breaking force (Yang *et al.* [93] also reported the usefulness of speed feedback in end-to-end driving). Experiments are performed in CARLA for different traffic situations (including other vehicles and pedestrians), lighting and weather conditions. The overall approach is termed as conditional imitation learning (CIL). In fact, already cited Muller *et al.* and Sauer *et al.* leveraged from CIL to elaborate their own proposals. Liang *et al.* [73] also use CIL as imitation learning stage before refining the resulting model by applying reinforcement learning. Wang *et al.* [72] use CIL too, but incorporating ego-vehicle heading information as the same CNN layer level than speed.

Overall, all these works mainly focus on vision-based end-

to-end driving. In this paper, we explore multimodal end-to-end driving using RGB and depth as raw data. Note that this can be complementary to most of the cited papers. Without losing generality, we chose CIL as core CNN architecture due to its effectiveness and increasing use.

Focusing on multimodality, Sobh *et al.* [95] have used CARLA to propose a CIL-based driving approach modified to process camera and LiDAR data. In this case, the information fusion is done by a mid-level approach; in particular, before fusion, RGB images are used to generate a semantic segmentation which correspond to one of the information streams reaching the fusion layers, and there are two more independent streams based on LiDAR, one encoding a bird view and the other a polar grid mapping. Khan *et al.* [96] also used CARLA to propose an end-to-end driving CNN based on RGB and depth images, which predicts only the steering angle, assuming that neither other vehicles nor pedestrians are present. In a first step, the CNN is trained only using depth information (taken as the Z-buffer produced by UE4², the game engine behind CARLA). This CNN has an initial block of layers (CNN encoder) that outputs depth-based features, which are later used to predict the steering angle with a second block of fully connected layers. In a second step, this angle-prediction block is discarded and replaced by a new fully connected one. This new block relies on the fusion of the depth-based features and a semantic segmentation produced by a new CNN block that processes the RGB image paired with the depth image. During training, semantic segmentation is conditioned to depth-based features due to the fusion block and back-propagation. This approach can be considered a type of mid-level fusion.

In contrast to these multimodal end-to-end driving approaches, we assess early, mid and level fusion schemes without forcing intermediate representations which are not necessarily trivial to obtain (*e.g.* semantic segmentation is an open problem in itself). In fact, we will see that we obtain best results under early fusion. In all cases, we run the standard CARLA benchmark [98], *i.e.* including dynamic actors (vehicles and pedestrians), and generalization to an unseen town and new weathers. Overall, we will see that CIL and early fusion provide results at state-of-the-art level.

III. MULTIMODAL FUSION

In this section we first detail CIL architecture [71], and then show how we have adapted it to leverage from multimodal perception data.

A. Base CIL architecture

Fig. 1 shows the CNN architecture implementing CIL. The observations (CIL's input) are twofold, namely, sensorial perception data, \mathbf{p} , and vehicle state measurements, \mathbf{m} . The action (CIL's output), \mathbf{a} , consists of vehicle controls determining the desired vehicle maneuver. CIL includes a CNN block to extract perception features, $P(\mathbf{p})$; as well as a block of fully connected layers to extract measurement features $M(\mathbf{m})$. A joint layer of features is formed by appending

²www.unrealengine.com

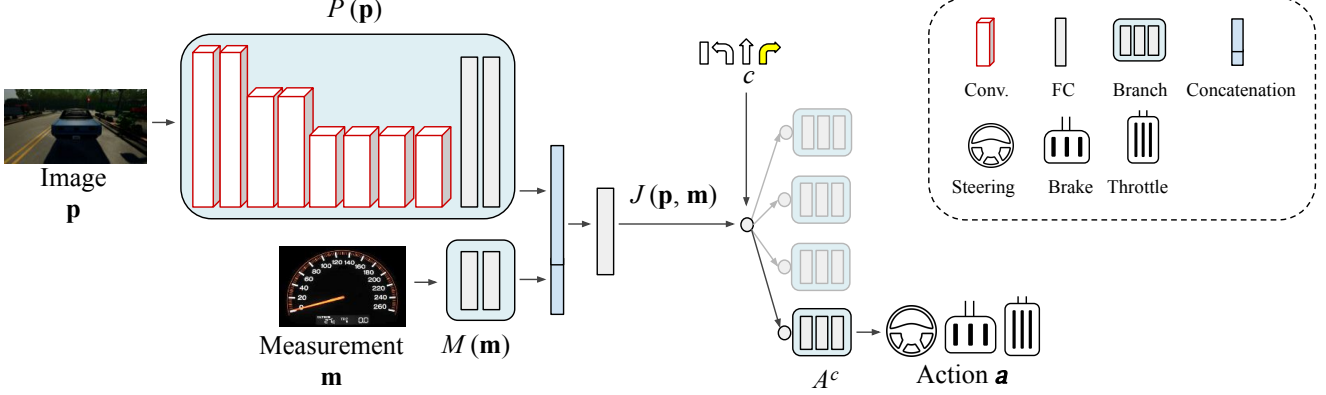


Fig. 1. CIL branched architecture: vehicle maneuvers (actions) in the form of the triplet \langle steering angle, throttle, brake \rangle , depend on a high-level route navigation command (branch selector) running on $\{\text{turn-left}, \text{turn-right}, \text{go-straight}, \text{continue}\}$, as well as on the world observations in the form of perception data (e.g. an RGB image) and vehicle state measurements (e.g. speed).

$P(\mathbf{p})$ and $M(\mathbf{m})$; which is further processed by a new fully connected layer (could be more if required) to obtain the joint features $J(\langle P(\mathbf{p}), M(\mathbf{m}) \rangle)$, or just $J(\mathbf{p}, \mathbf{m})$ simplifying the notation. Up to this point of the overall neural network, the processing done with the observations is considered common to any driving maneuver/action. However, many times, the autonomous vehicle reaches ambiguous situations which require to incorporate informed decisions. For instance, when reaching a cross intersection, without incorporating a route navigation command (e.g. from a global trajectory plan, or as a passenger order), the vehicle could only take a random decision about turning to the left or to the right, or just going straight. Therefore, it is important that the end-to-end driving CNN allows to incorporate high-level commands, c , such as '*in the next intersection turn left*', or '*turn right*', or just '*go straight*'. Moreover, a will take very different values depending on c . Thus, provided c takes discrete values, having specialized neural network layers for each maneuver can be also more accurate a priori. All this is achieved in the CIL proposal by incorporating fully connected maneuver/action branches, A^c , selected by c (both during CNN training and vehicle self-driving).

Table V details parameters of the CIL architecture used in [71], which are the ones we follow here too. In this case, \mathbf{p} is a RGB image of 200×88 pixels and 8 bpp at each color channel, \mathbf{m} is a real value with the current speed of the vehicle, and \mathbf{a} consists of three real-valued signals that set the next maneuver in term of steering angle, throttle, and brake. Thus, the idea was to perform vision-based self-driving, as well as taking into account the vehicle speed to apply higher/lower throttle and brake for the same perceived traffic situation. In [71], the focus is on handle intersections, then the considered c values are $\{\text{turn-left}, \text{turn-right}, \text{go-straight}, \text{continue}\}$, where the last refers to just keep driving in the current lane and the others inform about what to do when reaching next intersection (which is an event detected by the own CNN, no metric information is required). Accordingly, there are four branches A^c . Therefore, if we term by F the end-to-end driver, we have $F(\mathbf{p}, \mathbf{m}, c) = A^c(J(\mathbf{p}, \mathbf{m}))$. As shown, in [71], this manner of

explicitly taking into account high-level navigation commands is more effective than other alternatives.

B. Fusion schemes

Fig. 2 illustrates how we fuse RGB and depth information following mid, early and late fusion approaches.

a) *Early fusion*: In this case, with respect to the original CIL we only change the number of channels of \mathbf{p} ; *i.e.* from three (RGB) to four (RGBD) channels. The CIL network only changes the first convolutional layer of $P(\mathbf{p})$ to accommodate for the extra input channel, the rest of the network is equal than the original. Table V details CIL for early fusion (where no fusion are just special cases).

b) *Mid fusion*: In this case, we replicate twice the perception processing $P(\mathbf{p})$. One of the $P(\mathbf{p})$ blocks processes only RGB images, the other one only depth images. Then, we build the joint feature vector $\langle P(\text{RGB}), P(\text{D}), M(\mathbf{m}) \rangle$ which is further processed to obtain $J(\text{RGB}, \text{D}, \mathbf{m})$. From this point, the branched part of CIL is the same than in the original architecture. Table VI details CIL for mid fusion.

c) *Late fusion*: In this case, we replicate twice the full CIL architecture. One CIL processes the RGB channels and the other one the depth channel, only the measurements are shared as input. Therefore, we run $A^c(J(\text{RGB}, \mathbf{m}))$, as well as $A^c(J(\text{D}, \mathbf{m}))$; then, the two outputs of these CIL branches are concatenated and further processed by a module of fully connected layers, the output of which conveys the final action values. Note that this is a kind of mixture-of-experts approach, where the two experts are jointly trained. Table VII details CIL for late fusion.

As is common practice in the literature, in this paper we assume a pixel-level correspondence of all channels, and we also normalize all channels to be in the same magnitude range (here we normalize depth values to match the range of color channels, *i.e.* $[0 \dots 255]$). These points are needed for early fusion, while for mid and late fusion a priori is not strictly necessary. However, in order to make fair comparisons among these three fusion schemes, we input the same data in all

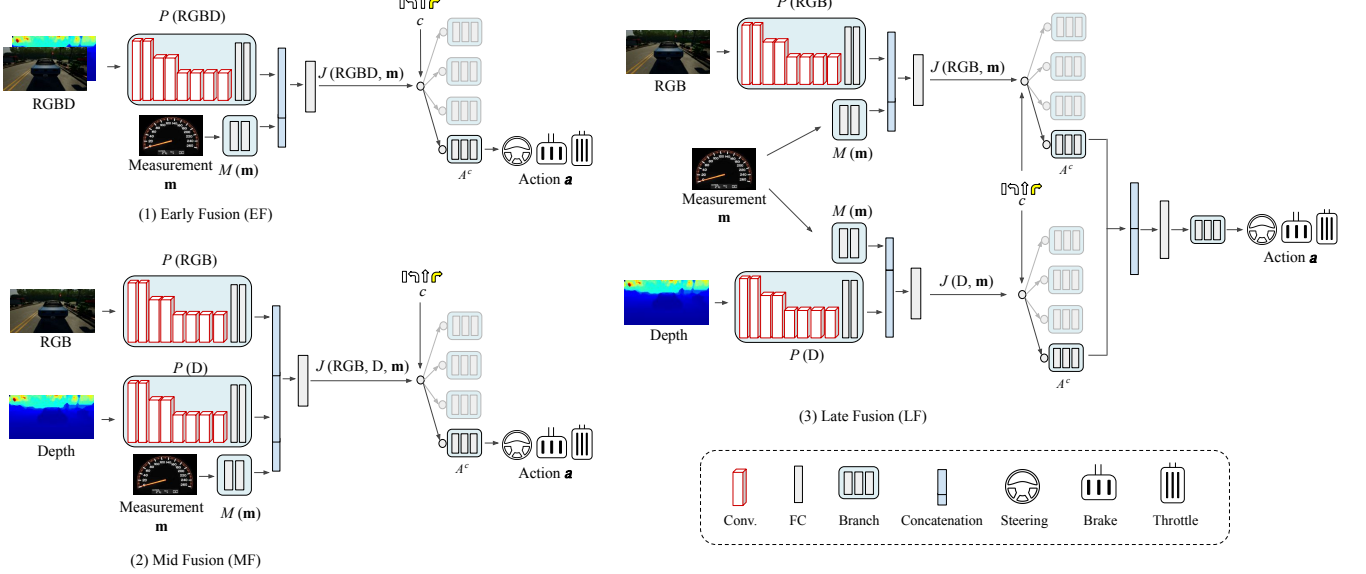


Fig. 2. Network Architectures - we explore RGBD from the perspective of early, mid and late fusion of the RGB and Depth (D) modalities. (1) Early Fusion: the raw RGB and D data are fused at the input of the CIL architecture; (2) Mid Fusion: intermediate CIL feature layers from RGB and D streams are fused; (3) Late Fusion: the output (maneuver commands) of the RGB and D CIL architecture are fused to output the final values after further neural processing.

experiments. Note also, than from the computational point of view early fusion is more efficient than mid and late fusion in terms of processing power and memory requirements, both at training and testing time.

C. Loss function

Given a predicted action \mathbf{a} , a ground truth action \mathbf{a}^{gt} , and a vector of weights \mathbf{w} , we use L1 loss function, which is defined as $\ell_{act}(\mathbf{a}, \mathbf{a}^{gt}, \mathbf{w}) = \sum_i^n |w_i(a_i - a_i^{gt})|$. In this case, $n = 3$ (steering angle, throttle, brake). Note that when computing \mathbf{a} , only one A^c branch is active at a time. In particular, the one selected by the particular command c associated to the current input data (\mathbf{p}, \mathbf{m}). We make this fact explicit by changing the notation to $\ell_{act}(\mathbf{a}, \mathbf{a}^{gt}, \mathbf{w}; c)$.

In addition, as in other computer vision problems addressed by deep learning [103], [104], we empirically found that using multitask learning helps to obtain more accurate CIL networks. In particular, we add an additional branch of three fully connected layers to predict current vehicle speed from the perception data features $P(\mathbf{p})$, see ‘Speed Branch’ in Table V, Table VI, and Table VII. This prediction relies on a L1 loss $\ell_{sp}(s, s^{gt}) = |s - s^{gt}|$, where s is the predicted speed and s^{gt} is the ground truth speed which, in this case, is already available since it corresponds to the measurement used as input. We remark that speed prediction is only used at training time.

Thus, all networks, *i.e.* both single- and multimodal, are trained according to the same total loss $\ell(\mathbf{a}, \mathbf{a}^{gt}, \mathbf{w}; c; s, s^{gt}) = \beta \ell_{act}(\mathbf{a}, \mathbf{a}^{gt}, \mathbf{w}; c) + (1 - \beta) \ell_{sp}(s, s^{gt})$, where β is used to balance the relevance of ℓ_{act} and ℓ_{sp} losses.

IV. EXPERIMENTS

A. Dataset

In order to conduct our experiments, we will rely on the open source driving simulator known as CARLA [98]. There are several reasons for this. First, carrying such a study on real AVs is prohibitively expensive for most research teams; in fact, one of the goals of CARLA is democratizing research on AVs and conclusions based on thousands of experiments in CARLA can later be efficiently translated to real environments [71]. Second, due to this, many recent previous works on end-to-end driving [71], [68], [67], [69], [72], [73], [80] already rely on the standard benchmark provided in the CARLA environment; thus, we will be able to compare our results with the previous literature. Third, it has been shown [101] that even for visuomotor models, it is still necessary to develop new metrics for offline evaluation (*i.e.* based on static datasets) of end-to-end driving models, so that they correlate better with actual driving; therefore, it is really important to evaluate these driving models in an on-board driving regime, which is possible in a realistic simulator such as CARLA. Fourth, it seems that for some scenarios the end-to-end paradigm may need exponentially more training samples than the modular one [105], so there is a trade-off between collecting driving runs (for the end-to-end paradigm) and manually annotating on-board acquired data (for the modular paradigm) which, together with the gigantic effort needed to demonstrate that an AV outperforms human drivers, really encourages to rely on simulators during the development of AI drivers [106] (as well as methods of curriculum learning and novelty detection in end-to-end driving [107], [108], which are complementary but out-of-scope topics with respect to the work presented in this paper).

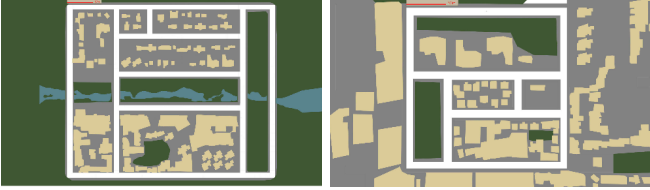


Fig. 3. Bird-view road maps of Town 1 (left) and Town 2 (right).

TABLE I

TRAINING, VALIDATION, AND TESTING SETTINGS. TRAINING IS BASED ON A PRE-RECORDED DATASET. VALIDATION AND TESTING ARE BASED ON ACTUAL DRIVING EPISODES.

| | Training (dataset) | Validation (episodes) | Testing (episodes) |
|-------------------|-----------------------|--------------------------|-----------------------|
| Wet cloudy noon | Town 1 | Towns 1 & 2 | Towns 1 & 2 |
| Soft rainy sunset | | | |
| Clear noon | | | |
| Clear after rain | | | |
| Clear sunset | | | |
| Heavy rain noon | | | |

For our experiments, we follow standard practices when training and testing AI drivers in CARLA (0.8.2 version). It contains two towns (Fig. 3), Town 1 and Town 2, which contain two-directional roads with curves and intersections, buildings, vegetation, urban furniture, traffic signs, traffic lights, and dynamic traffic participants such as other vehicles and pedestrians. Town 1 deploys 2.9Km of road and 11 intersections, while Town 2 contains 1.4Km of road and 8 intersections. The different towns can be travelled under different weather conditions (Fig. 4): ‘clear noon’, ‘clear after rain’, ‘heavy rain noon’, and ‘clear sunset’, ‘wet cloudy noon’ and ‘soft rainy sunset’. Table I shows how these towns and weathers are normally used [98] for training, validation and testing; where, irrespective of the town and weather condition, validation and testing is always based on driving runs, not in pre-recorded datasets, while training requires pre-recording a dataset. Validation is performed to select a driving model among those trained as different trials from the same training dataset, while testing is performed for benchmarking the selected models. Note that Town 2 is used for validation and testing, but not for training. weathers ‘clear after rain’, ‘heavy rain noon’, and ‘clear sunset’ are used both in training and testing, but not in validation. Weather ‘soft rainy sunset’ is used in validation and testing but not in training, and ‘wet cloudy noon’ is used only for testing.

In order to train our CNNs, we have used the same dataset than in [101] since it corresponds to 25h of driving in Town 1, balancing the training weathers. Briefly, this dataset was collected by a hard-coded auto-pilot with access to all the privileged information of CARLA required for driving like an expert. The auto-pilot kept a constant speed of 35 km/h when driving straight and reduced the speed when making turns. The state of the traffic lights was not considered by the auto-pilot, but it was by the rest of vehicles; thus, in this work we do not aim at respecting traffic lights. Images were recorded at 10fps from three cameras: a central forward-facing one and

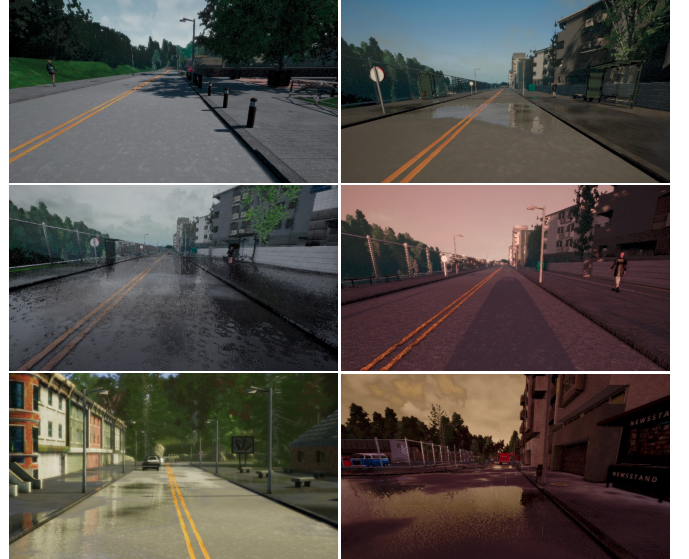


Fig. 4. Top, from Town 1: clear noon (left) and clear after rain (right). Middle, from Town 1: heavy rain noon (left) and clear sunset (right). Bottom, from Town 2: wet cloudy noon (left) and soft rainy sunset (right).

two lateral cameras facing 30° left and right. The central camera is the only one used for self-driving, while the images coming from the lateral cameras are used only at training time to simulate episodes of recovering from driving errors as can be done with real cars [64] (the protocol for injecting noise follows [71]). Overall, the dataset contains ~ 2.5 millions of RGB images of 800×600 pixels resolution, with associated ground truth (see Fig. 5) consisting of corresponding images of dense depth and pixel-wise semantic classes (semantic segmentation), as well as meta-information consisting of the high-level commands provided by the navigation system (continue in lane, in next intersection go straight, turn left or turn right), and car information such as speed, steering angle, throttle, and braking. In this work we want to use perfect semantic segmentation to develop an upper-bound driver. Since we are focusing on end-to-end driving, the twelve semantic classes of CARLA have been mapped here to five that we consider sufficient to develop such upper-bound. In particular, we keep the original *road-surface*, *vehicle*, and *pedestrian*, while *lane-marking* and *sidewalk* are mapped as *lane-limits* (Town 1 and Town 2 only have roads with one go and one return lane, separated by double continuous lines), and the remaining seven classes are mapped as *other*. Figure 5 shows an example.

Focusing on depth information, as is common in the literature, we assume that RGB images can have associated dense depth information; for instance, Premebida *et al.* [109] obtain it from LiDAR point clouds. In CARLA, the depth ground truth is extremely accurate since it comes directly from the Z-buffer used during simulation rendering. In particular, depth values run from 0 to 1,000 meters and are codified with 24 bits, which means that depth precision is of $\sim 1/20\text{mm}$. This distance range coverage and depth precision is far beyond from what even *active* sensors can provide. Therefore, we post-process depth data to make it more realistic. In particular, we take as a realistic sensor reference the Velodyne information

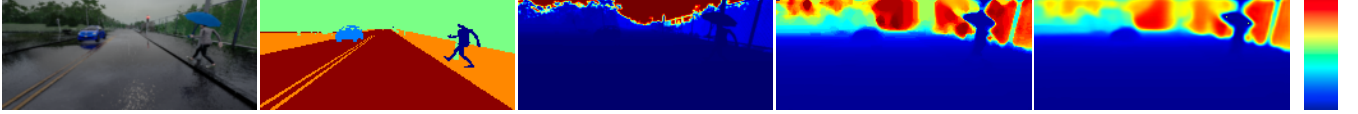


Fig. 5. From left to right: original RGB image, semantic segmentation ground truth (for the five considered classes), CARLA depth ground truth, post-processed to be closer to the capabilities of an *active* depth Sensor, and monocular depth estimation from a model trained using such a depth.

of KITTI dataset [83]. First we trim depth values to consider only those within the 1 to 100 meters interval, *i.e.* pixels of the depth image with values outside this range are considered as not having depth information. Second, we re-quantify the depth values to have an accuracy of $\sim 4\text{cm}$. Third, we perform inpainting to fill-in the pixels with no information. Finally, we apply a median filter to avoid having perfect depth boundaries between objects. The new depth images are used both during training and testing. Fig. 5 shows an example of a depth image from CARLA and its corresponding post-processed version.

B. Training protocol

All CIL models presented in this work rely on the same training protocol, partially following [71]. In all our CIL models original sensor channels (R/G/B/D) are first trimmed to remove sky and very close areas (top and bottom part of the channels), and then down-scaled to finally obtain channels of 200×88 pixel resolution. In our initial experiments we found that traditional photometric and geometric recipes for data augmentation were not providing better driving models, thus, we did not use them in this paper. Drop-out is not used in convolutional layers, but it is used in some fully connected layers as detailed in the supplementary material (Tables V, VI, VII).

During a training run we use Adam optimizer with 120 training samples per iteration (minibatch) and an initial learning rate of 0.0002, decreasing to the half each 50,000 iterations. Minibatches are balanced in terms of per A^c branch samples. Moreover, we use $\mathbf{w} = (0.5, 0.45, 0.05)$ to weight the relevance of the control signals (action) in the loss function, and action and speed losses are balanced according to $\beta = 0.95$. In order to select the best intermediate model of a training run, we perform 500,000 iterations monitoring a validation performance measurement, V_P , each 100,000 iterations (thus, five times). The intermediate model with highest V_P is selected as the resulting model of the training run. Since CIL models are trained from the scratch, variability is expected in their performance. Thus, for each type of model we perform five training runs, finally selecting the model with the highest V_P among those resulting from the five training runs.

We use a V_P value that balances training-validation differences in terms of town and weather conditions. In particular, we use $V_P = 0.25V_w + 0.25V_t + 0.50V_{wt}$; where V_w is the success rate when validating in Town 1 and ‘soft rainy sunset’ weather (not included in training data), V_t is a success rate when validating in Town 2 (not included in training data) and ‘clear noon’ weather (on one of the included in training data), and V_{wt} means stands for a success rate when validating in Town 2 and ‘soft rainy sunset’ (neither town, nor weather are

part of the training data). In all these validation conditions, the success rate is defined as the number of successful episodes over the total number of ran episodes. Episodes and their success are defined according to the standard CARLA benchmark [98]. Briefly, the total number of episodes to try in each driving condition is 25, where each episode has a starting location and a destiny (a global planner provides the topological route for the driving), and the episode is completed successfully if the vehicle reaches the destiny within a preset time.

C. Testing protocol

In fact, as testing protocol we run the standard CARLA benchmark where the driving conditions (town and weather) are defined as four main blocks (use Table I as reference): (1) driving in the same conditions of the training set (something that is common practice when developing real autonomous vehicles); (2) driving in the town included in the training set (Town 1), but with weather conditions not in the training set; (3) driving in a town not included in the training set (Town 2), but with the same weather conditions of the training set; (4) driving in conditions not included in the training set. These four blocks are termed as *Training Conditions*, *New Town*, *New Weather*, and *New Town & Weather*, respectively. For each condition, the CARLA driving benchmark allows to set 4 tasks of increasing difficulty:

- *Straight*: the goal is straight ahead of the starting position.
- *One turn*: reaching the goal requires one turn, left or right.
- *Navigation*: reaching the goal requires an arbitrary number of turns.
- *Navigation with dynamic obstacles*: as previous task, with other vehicles and pedestrians moving around.

D. Experimental Results

We start the analysis of the experimental results by looking at Table II, which is produced during training and selection of the best CIL networks. We focus first on RGB data as well as depth based on the post-processed CARLA depth ground truth, termed here as *active* depth (Sect. IV-A) since its accuracy and covered depth range is characteristic of active sensors (*e.g.* LiDAR). We see that the best (among five training runs) validation performance V_P is 48% when using RGB data only. So we will use the corresponding CIL model as RGB-based driver in the following experiments. Analogously, for the case of using only active depth (D), the best CIL reports a performance of 74%. The best performances for early fusion (EF), mid fusion (MF), and late fusion (LF) are 91%, 74% and 67%, respectively. Again, we take the corresponding CIL models as drivers for the following experiments.

TABLE II

V_P FOR FIVE TRAINING RUNS (%) BASED ON RGB ONLY, DEPTH (D) ONLY, AND RGBD COMBINED BY EARLY FUSION (EF), MID FUSION (MF), OR LATE FUSION (LF). DEPTH CAN COME FROM AN ACTIVE SENSOR, OR BE ESTIMATED FROM RGB IMAGES (MONO-DEPTH ESTIMATION).

| | RGB | | Active | | Estimation | |
|---|-----------|-----------|-----------|-----------|------------|-----------|
| | D | EF | MF | LF | D | EF |
| 1 | 48 | 74 | 91 | 61 | 60 | 51 |
| 2 | 36 | 67 | 71 | 71 | 63 | 49 |
| 3 | 46 | 73 | 75 | 58 | 67 | 46 |
| 4 | 40 | 68 | 71 | 74 | 60 | 59 |
| 5 | 36 | 68 | 77 | 52 | 62 | 51 |
| | | | | | | 49 |

Table III reports the performance of the selected RGB/D/RGBD CIL models according to CARLA benchmark. We have also included a model trained on perfect semantic segmentation (SS) according to the five classes considered here for self-driving (see Fig. 5). In other words, instead of RGB/D/RGBD, the input to this CIL model is such a perfect SS provided by CARLA. Thus, we consider this SS-based CIL model as an upper bound. Indeed, its reported performance is most of the times ≥ 96 , reaching 100 several times. This also confirms that the CIL model is able to drive properly in CARLA conditions provided there is a proper input. We can see that, indeed, active depth is a powerful information for end-to-end driving by itself, outperforming RGB. However, in most of the cases RGBD outperforms the use of only RGB or only D. The most clear case is for new town and weather with dynamic objects, *i.e.* for the most challenging conditions, where RGB alone reaches a success rate of 44, D alone 68, but together the success rate is 94 for early fusion. In fact, mid and late fusion also outperform single-modal models. When evaluating in the training town (*i.e.* in training conditions and new weather) with dynamic objects, late fusion outperforms early fusion, but both outperform single-modal models. However, for a new town (irrespective of the weathers) early fusion clearly outperforms mid and late fusion, these two reporting similar performance. In any case, it is clear that multimodality improves CIL performance with respect to a single modality, which is the main question we wanted to answer in this paper.

In order to further analyse the goodness of multimodality, we confront it to other single-modal methods of the state-of-the-art (see Sect. II). Not all the corresponding papers provide details about the training methodology or training datasets; thus, this comparison is solely based on the reported performances on CARLA benchmark and must be taken only as an additional reference about the goodness of multimodality. Early fusion, is the smaller CNN architecture in terms of weights, thus, we are going to focus on it for this comparison. Table III plots the results. MP and RL stand for modular perception and reinforcement learning, respectively. The reported results are reproduced from [98]. CAL stands for conditional affordance learning and the results are reproduced from [67]. CIRL stands for controllable imitative reinforcement learning

and the results are reproduced from [73]. Finally, MT stands for multitask learning, and the results are reproduced from [80]. We see how, in presence of dynamic traffic participants, irrespective of the towns and weather conditions the RGBD early fusion (with active depth) is the model with higher success rate on the CARLA benchmark. On the other hand, such an early fusion approach can be combined with CAL or CIRL methods, they are totally compatible. Overall, this comparison with the state-of-the-art reinforces the idea that multimodality can help end-to-end driving.

Once it is clear that multimodality is an approach worth to follow within the end-to-end driving paradigm, we can rise the question of whether monocular depth estimation [41], [110], [111], [42] can be as effective as depth coming from active sensors in this context. In the former case, it would consists on a multisensory multimodal approach, while the later case would correspond to a single-sensor multimodal approach since both RGB and depth come from the same camera sensor (depth is estimated from RGB). In order to carry out a proof-of-concept, we have used our own monocular depth estimation model [42] (it was state-of-the-art at the moment of its publication) fine-tuned on CARLA training data. More specifically, the same dataset used for training the multimodal CIL models have been used to fine-tune our monocular depth estimation model, *i.e.* using the post-processed depth channels and corresponding RGB images. During training, we monitored the regression loss until it was stable, we did not stopped training based on the performance on validation episodes. In this way, the resulting monocular depth estimation model can be seen as an off-the-shelf one and, thus, perform a fair comparison with active depth (which comes also off-the-shelf). Figure 5 shows and example of monocular depth estimation.

Analogously to the experiments shown so far, we trained a CIL model based on the estimated depth as well as on the corresponding multimodal (RGBD) fusion. In order to reduce the burden of experiments, we have used early fusion since it was the best performing for the active depth case. The training performances for model selection can be seen in Table II. We selected the CIL models of V_P 59 and 51, respectively. In validation terms, such performances are already clearly worse than the analogous based on active depth. Table III shows the results on the CARLA benchmark. Indeed, these are worse than using active depth, however, still when remaining in the training town (both for training and new weather) monocular-based EF outperforms the corresponding depth and RGB alone, especially in the most challenging case of navigation in presence of dynamic objects. This is not the case when we keep the training weather but change the town. Monocular depth does not performs as well in this case, and so happens to EF. We think this is due to lack of generalization in the depth estimation itself. However, when evaluating in a new town and weather, again monocular-based EF outperforms the corresponding depth and RGB alone, we think because monocular depth estimation is adding robustness against adverse weather conditions. Overall, we think that this single-sensor multimodal setting is really worth to pursue. Moreover, although it is out of the scope of this paper, we think

TABLE III
SUCCESS RATE (%) ON CARLA BENCHMARK. CIL BASED ON PERFECT SEMANTIC SEGMENTATION (SS) ACTS AS UPPER BOUND (NOT SHOWN IN BOLD).

| Task | SS | RGB | D | Active | | | Estimated | | SS | RGB | D | Active | | | Estimated | |
|---------------------|-----|-----|------------|-----------|----|-----------|-----------|-----------|-----|-----|-----------|-----------|----|-----------|-----------|----|
| | | | | EF | MF | LF | D | EF | | | | MF | LF | D | EF | MF |
| Training Conditions | | | | | | | | | | | | | | | | |
| Straight | 97 | 96 | 100 | 99 | 90 | 99 | 93 | 98 | 100 | 82 | 94 | 96 | 86 | 77 | 77 | 74 |
| One turn | 100 | 95 | 92 | 99 | 91 | 90 | 86 | 96 | 96 | 69 | 72 | 81 | 79 | 61 | 47 | 48 |
| Navigation | 96 | 87 | 91 | 92 | 90 | 93 | 76 | 94 | 96 | 63 | 84 | 90 | 80 | 52 | 49 | 46 |
| Nav.Dynamic | 91 | 84 | 83 | 89 | 80 | 92 | 70 | 91 | 100 | 57 | 71 | 87 | 76 | 57 | 47 | 46 |
| New Weather | | | | | | | | | | | | | | | | |
| Straight | 100 | 84 | 98 | 96 | 98 | 96 | 90 | 86 | 100 | 84 | 98 | 96 | 88 | 98 | 78 | 90 |
| One turn | 100 | 78 | 96 | 92 | 92 | 94 | 92 | 80 | 96 | 76 | 74 | 84 | 66 | 66 | 62 | 68 |
| Navigation | 96 | 74 | 88 | 90 | 94 | 96 | 72 | 76 | 96 | 56 | 86 | 90 | 78 | 74 | 50 | 62 |
| Nav.Dynamic | 92 | 66 | 90 | 90 | 78 | 96 | 80 | 84 | 98 | 44 | 68 | 94 | 76 | 76 | 50 | 52 |

TABLE IV
SUCCESS RATE (%) COMPARISON WITH THE STATE-OF-THE-ART ON CARLA BENCHMARK (SEE MAIN TEXT FOR DETAILS).

| Task | MP | RL | CAL | CIRL | MT | Active-EF | | MP | RL | CAL | CIRL | MT | Active-EF | | |
|-------------|------------|----|------------|------------|------------|-----------|------------|----|----|-----------|------------|------------|-----------|------|--|
| | | | | | | Training | Conditions | | | | | | New | Town | |
| Straight | 98 | 89 | 100 | 98 | 98 | 99 | 99 | 92 | 74 | 93 | 100 | 100 | 96 | | |
| One turn | 82 | 34 | 97 | 97 | 87 | 99 | | 61 | 12 | 82 | 71 | 81 | | 81 | |
| Navigation | 80 | 14 | 92 | 93 | 81 | 92 | | 24 | 3 | 70 | 53 | 72 | 90 | | |
| Nav.dynamic | 77 | 7 | 83 | 82 | 81 | 89 | | 24 | 2 | 64 | 41 | 53 | 87 | | |
| New Weather | | | | | | | | | | | | | | | |
| Straight | 100 | 86 | 100 | 100 | 100 | 96 | | 50 | 68 | 94 | 98 | 96 | 96 | | |
| One turn | 95 | 16 | 96 | 94 | 88 | 92 | | 50 | 20 | 72 | 82 | 82 | 84 | | |
| Navigation | 94 | 2 | 90 | 86 | 88 | 90 | | 47 | 6 | 68 | 68 | 78 | 90 | | |
| Nav.dynamic | 89 | 2 | 82 | 80 | 80 | 90 | | 44 | 4 | 64 | 62 | 62 | 94 | | |

that performing end-to-end driving may be a good protocol for evaluating depth estimation models beyond static metrics currently used, which are agnostic to the task in which depth estimation is going to be used. Note that even for evaluating the driving performance of end-to-end driving models in itself, it has been shown that relying only on static evaluations may be misleading [101].

V. CONCLUSION

In this paper we have confronted single- and multimodal perception data in the task of end-to-end driving by imitation learning. As multi-modality perception data we have focused on RGB and depth, since they are usually available in autonomous vehicles through the presence of cameras and active sensors such as LiDAR. As end-to-end driving model we have used branched conditional imitation learning (CIL). Relying on a well-established simulation environment, CARLA, we have assessed the driving performance of single-modal (RGB, depth) CIL models, as well as multimodal CIL models according to early, mid, and late fusion paradigms. In all cases, the depth information available in CARLA was post-processed to obtain a more realistic range of distances and depth accuracy. This depth was also used to train a depth estimation model so that the experiments have covered multimodality not only based on a multisensory setting (RGB and active depth) but also based on a single-sensor setting (RGB and estimated depth). Overall, the experiments clearly allow us to conclude that multimodality (RGBD) is indeed a

beneficial approach for end-to-end driving. In fact, we plan to follow this line of work in the near future, focusing on the single-sensor setting since better estimation models are required in order to compete with the multisensory setting.

REFERENCES

- [1] U. Franke, "Autonomous driving," in *Computer Vision in Vehicle Technology*, 2017.
- [2] J. Janai, F. Güney, A. Behl, and A. Geiger, "Computer vision for autonomous vehicles: Problems, datasets and state-of-the-art," arXiv:1704.05519, 2017.
- [3] B. Paden, M. Cáp, S. Z. Yong, D. S. Yershov, and E. Frazzoli, "A survey of motion planning and control techniques for self-driving urban vehicles," *IEEE Trans. on Intelligent Vehicles*, vol. 1, no. 1, pp. 33–55, 2016.
- [4] W. Schwarting, J. Alonso, and D. Rus, "Planning and decision-making for autonomous vehicles," *Annual Reviews of Control, Robotics, and Autonomous Systems*, vol. 1, pp. 187–210, May 2018.
- [5] S. Ren, K. He, R. Girshick, and J. Sun, "Faster R-CNN: towards real-time object detection with region proposal networks," in *Neural Information Processing Systems (NIPS)*, 2015.
- [6] W. Liu, D. Anguelov, D. Erhan, C. Szegedy, S. Reed, C.-Y. Fu, and A. Berg, "SSD: single shot multibox detector," in *European Conference on Computer Vision (ECCV)*, 2016.
- [7] J. Redmon and A. Farhadi, "YOLO9000: better, faster, stronger," in *Int. Conf. on Computer Vision and Pattern Recognition (CVPR)*, 2017.
- [8] F. Chabot, M. Chaouch, J. Rabarisoa, C. Teuliére, and T. Chateau, "Deep MANTA: A coarse-to-fine many-task network for joint 2D and 3D vehicle analysis from monocular image," in *Int. Conf. on Computer Vision and Pattern Recognition (CVPR)*, 2017.
- [9] A. Mousavian, D. Anguelov, J. Flynn, and J. Kosecka, "3D bounding box estimation using deep learning and geometry," in *Int. Conf. on Computer Vision and Pattern Recognition (CVPR)*, 2017.

[10] A. H. Lang, S. Vora, H. Caesar, L. Zhou, J. Yang, and O. Beijbom, “PointPillars: Fast encoders for object detection from point clouds,” arXiv:1812.05784, 2018.

[11] M. Simon, S. Milz, K. Amende, and H. Gross, “Complex-YOLO: Real-time 3D object detection on point clouds,” arXiv:1803.06199, 2018.

[12] B. Yang, W. Luo, and R. Urtasun, “PIXOR: Real-time 3D object detection from point clouds,” in *Int. Conf. on Computer Vision and Pattern Recognition (CVPR)*, 2018.

[13] Y. Zhou and O. Tuzel, “VoxelNet: End-to-end learning for point cloud based 3D object detection,” in *Int. Conf. on Computer Vision and Pattern Recognition (CVPR)*, 2018.

[14] C. R. Qi, W. Liu, C. Wu, H. Su, and L. J. Guibas, “Frustum PointNets for 3D object detection from RGB-D data,” in *Int. Conf. on Computer Vision and Pattern Recognition (CVPR)*, 2018.

[15] Y. Yan, Y. Mao, and B. Li, “SECOND: Sparsely embedded convolutional detection,” *Sensors*, vol. 18, no. 10, 2018.

[16] A. multilevel mixture-of-experts framework for pedestrian classification, “Markus enzweiler and Dariu M. gavrila,” *IEEE Trans. on Image Processing*, vol. 20, no. 10, pp. 2967–2979, 2011.

[17] A. González, D. Vázquez, A. M. López, and J. Amores, “On-board object detection: Multicue, multimodal, and multiview random forest of local experts,” *IEEE Trans. on Cybernetics*, vol. 47, no. 11, pp. 3980–3990, 2017.

[18] X. Chen, H. Ma, J. Wan, B. Li, and T. Xia, “Multi-view 3D object detection network for autonomous driving,” in *Int. Conf. on Computer Vision and Pattern Recognition (CVPR)*, 2017.

[19] A. Asvadi, L. Garrote, C. Premebida, P. Peixoto, and U. J. Nunes, “Multimodal vehicle detection: fusing 3D-LIDAR and color camera data,” *Pattern Recognition Letters*, vol. 115, pp. 20–29, November 2018.

[20] J. Ku, M. Mozifian, J. Lee, A. Harakeh, and S. Waslander, “Joint 3D proposal generation and object detection from view aggregation,” in *Int. Conf. on Intelligent Robots and Systems (IROS)*, 2018.

[21] A. Pfeuffer and K. Dietmayer, “Optimal sensor data fusion architecture for object detection in adverse weather conditions,” in *International Conference on Information Fusion (FUSION)*, 2018.

[22] C. Li, D. Song, R. Tong, and M. Tang, “Illumination-aware Faster R-CNN for robust multispectral pedestrian detection,” *Pattern Recognition*, vol. 85, pp. 161–171, January 2019.

[23] Y. Wu, H. Qin, T. Liu, H. Liu, and Z. Wei, “A 3d object detection based on multi-modality sensors of usv,” *Applied Sciences*, vol. 9, no. 3, 2019.

[24] D. Ponsa, A. M. López, J. Serrat, F. Llumbreras, and T. Graf, “Multiple vehicle 3D tracking using an unscented kalman,” in *Intelligent Transportation Systems Conference (ITSC)*, 2005.

[25] D. Mitzel and B. Leibe, “Taking mobile multi-object tracking to the next level: People, unknown objects, and carried items,” in *European Conference on Computer Vision (ECCV)*, 2012.

[26] W. Choi, “Near-online multi-target tracking with aggregated local flow descriptor,” in *International Conference on Computer Vision (ICCV)*, 2015.

[27] Y. Xiang, A. Alahi, and S. Savarese, “Learning to track: Online multi-object tracking by decision making,” in *International Conference on Computer Vision (ICCV)*, 2015.

[28] N. Wojke, A. Bewley, and D. Paulus, “Simple online and realtime tracking with a deep association metric,” in *International Conference on Image Processing (ICIP)*, 2017.

[29] G. Bhat, J. Johander, M. Danelljan, F. S. Khan, and M. Felsberg, “Unveiling the power of deep tracking,” in *European Conference on Computer Vision (ECCV)*, 2018.

[30] S. Sharma, J. A. Ansari, J. K. Murthy, and K. M. Krishna, “Beyond pixels: Leveraging geometry and shape cues for online multi-object tracking,” in *International Conference on Robotics and Automation (ICRA)*, 2018.

[31] M. Dimitrievski, P. Veelaert, and W. Philips, “Behavioral pedestrian tracking using a camera and LiDAR sensors on a moving vehicle,” *Sensors*, vol. 19, no. 2, 2019.

[32] Z. Zhu, D. Liang, S. Zhang, X. Huang, B. Li, and S. Hu, “Traffic-sign detection and classification in the wild,” in *Int. Conf. on Computer Vision and Pattern Recognition (CVPR)*, 2016.

[33] J. Long, E. Shelhamer, and T. Darrell, “Fully convolutional networks for semantic segmentation,” in *Int. Conf. on Computer Vision and Pattern Recognition (CVPR)*, 2015.

[34] H. Noh, S. Hong, and B. Han, “Learning deconvolution network for semantic segmentation,” in *International Conference on Computer Vision (ICCV)*, 2015.

[35] F. Yu and V. Koltun, “Multi-scale context aggregation by dilated convolutions,” in *International Conference on Learning Representation (ICLR)*, 2016.

[36] J. Uhrig, M. Cordts, U. Franke, and T. Brox, “Pixel-level encoding and depth layering for instance-level semantic labelling,” in *German Conference on Pattern Recognition (GCPR)*, 2016.

[37] M. Bai and R. Urtasun, “Deep watershed transform for instance segmentation,” in *Int. Conf. on Computer Vision and Pattern Recognition (CVPR)*, 2017.

[38] S. Liu, J. Jia, S. Fidale, and R. Urtasun, “SGN: sequential grouping networks for instance segmentation,” in *International Conference on Computer Vision (ICCV)*, 2017.

[39] L. Schneider, M. Jasch, B. Fröhlich, T. Weber, U. Franke, M. Pollefeys, and M. Rätsch, “Multimodal neural networks: RGB-D for semantic segmentation and object detection,” in *Scandinavian Conference on Image Analysis (SCIA)*, 2017.

[40] Q. Ha, K. Watanabe, T. Karasawa, Y. Ushiku, and T. Harada, “MFNet: Towards real-time semantic segmentation for autonomous vehicles with multi-spectral scenes,” in *Int. Conf. on Intelligent Robots and Systems (IROS)*, 2017.

[41] C. Godard, O. Aodha, and G. Brostow, “Unsupervised monocular depth estimation with left-right consistency,” in *Int. Conf. on Computer Vision and Pattern Recognition (CVPR)*, 2017.

[42] A. Gurram, O. Urfalioglu, I. Halfaoui, F. Bouzaraa, and A. M. Lopez, “Monocular depth estimation by learning from heterogeneous datasets,” in *Intelligent Vehicles Symposium (IV)*, 2018.

[43] Y. Gan, X. Xu, W. Sun, and L. Lin, “Monocular depth estimation with affinity, vertical pooling, and label enhancement,” in *European Conference on Computer Vision (ECCV)*, 2018.

[44] H. Fu, M. Gong, C. Wang, K. Batmanghelich, and D. Tao, “Deep ordinal regression network for monocular depth estimation,” in *Int. Conf. on Computer Vision and Pattern Recognition (CVPR)*, 2018.

[45] H. Badino, U. Franke, and D. Pfeiffer, “The stixel world - a compact medium level representation of the 3D-world,” in *DAGM: Joint Pattern Recognition Symposium*, 2009.

[46] L. Schneider, M. Cordts, T. Rehfeld, D. Pfeiffer, M. Enzweiler, U. Franke, M. Pollefeys, and S. Roth, “Semantic stixels: Depth is not enough,” in *Intelligent Vehicles Symposium (IV)*, 2016.

[47] M. Cordts, T. Rehfeld, L. Schneider, D. Pfeiffer, M. Enzweiler, S. Roth, M. Pollefeys, and U. Franke, “The stixel world: A medium-level representation of traffic scenes,” *Image and Vision Computing (IV)*, vol. 68, pp. 40–52, December 2017.

[48] D. Hernández-Juarez, L. Schneider, A. Espinosa, D. Vázquez, A. M. López, U. Franke, M. Pollefeys, and J. C. Moure, “Slanted Stixels: Representing San Francisco’s steepest streets,” in *British Machine Vision Conference (BMVC)*, 2017.

[49] R. Benenson, T. Radu, and L. V. Gool, “Stixels estimation without depth map computation,” in *International Conference on Computer Vision (ICCV) CVVT Workshop*, 2009.

[50] F. Brickwedde, S. Abraham, and R. Mester, “Mono-stixels: Monocular depth reconstruction of dynamic street scenes,” in *International Conference on Robotics and Automation (ICRA)*, 2018.

[51] F. Piewak, P. Pinggera, M. Enzweiler, D. Pfeiffer, and M. Zöllner, “Improved semantic stixels via multimodal sensor fusion,” arXiv:1809.08993, 2018.

[52] G. Ros, A. Sappa, D. Ponsa, and A. López, “Visual SLAM for driverless cars: A brief survey,” in *Intelligent Vehicles Symposium (IV) Workshops*, 2012.

[53] X. Zhang, A. B. Rad, and Y.-K. Wong, “Sensor fusion of monocular cameras and laser rangefinders for line-based simultaneous localization and mapping (slam) tasks in autonomous mobile robots,” *Sensors*, vol. 12, no. 1, pp. 429–452, 2012.

[54] G. Bresson, Z. Alsayed, L. Yu, and S. Glaser, “Simultaneous localization and mapping: A survey of current trends in autonomous driving,” *IEEE Trans. on Intelligent Vehicles*, vol. 2, no. 3, pp. 194–220, 2017.

[55] K. Tateno, F. Tombari, I. Laina, and N. Navab, “CNN-SLAM: Real-time dense monocular SLAM with learned depth prediction,” in *Int. Conf. on Computer Vision and Pattern Recognition (CVPR)*, 2017.

[56] X. Chen, H. Zhang, H. Lu, J. Xiao, Q. Qiu, and Y. Li, “Robust SLAM system based on monocular vision and LiDAR for robotic urban search and rescue,” in *Safety, Security and Rescue Robotics (SSRR)*, 2017.

[57] Y.-S. Shin, Y. S. Park, and A. Kim, “Direct visual SLAM using sparse depth for camera-LiDAR system,” in *International Conference on Robotics and Automation (ICRA)*, 2018.

[58] L. Li, Z. Liu, O. Ozgner, J. Lian, Y. Zhou, and Y. Zhao, “Dense 3D semantic SLAM of traffic environment based on stereo vision,” in *Intelligent Vehicles Symposium (IV)*, 2018.

[59] K. Qiu, Y. Ai, B. Tian, B. Wang, and D. Ca, "Siamese-ResNet: implementing loop closure detection based on siamese network," in *Intelligent Vehicles Symposium (IV)*, 2018.

[60] H. Yin, L. Tang, X. Ding, Y. Wang, and R. Xiong, "LocNet: global localization in 3D point clouds for mobile vehicles," in *Intelligent Vehicles Symposium (IV)*, 2018.

[61] J. Zhu, Y. Ai, B. Tian, D. Cao, and S. Scherer, "Visual place recognition in long-term and large-scale environment based on CNN feature," in *Intelligent Vehicles Symposium (IV)*, 2018.

[62] D. Pomerleau, "ALVINN: An autonomous land vehicle in a neural network," in *Neural Information Processing Systems (NIPS)*, 1989.

[63] Y. LeCun, U. Muller, J. Ben, E. Cosatto, and B. Flepp, "Off-road obstacle avoidance through end-to-end learning," in *Neural Information Processing Systems (NIPS)*, 2005.

[64] M. Bojarski, D. D. Testa, D. Dworakowski, B. Firner, B. Flepp, P. Goyal, L. D. Jackel, M. Monfort, U. Muller, J. Zhang, X. Zhang, J. Zhao, and K. Zieba, "End to end learning for self-driving cars," arXiv:1712.00409, 2016.

[65] H. Xu, Y. Gao, F. Yu, and T. Darrell, "End-to-end learning of driving models from large-scale video datasets," in *Int. Conf. on Computer Vision and Pattern Recognition (CVPR)*, 2017.

[66] C. Chen, A. Seff, A. L. Kornhauser, and J. Xiao, "DeepDriving: Learning affordance for direct perception in autonomous driving," in *International Conference on Computer Vision (ICCV)*, 2015.

[67] A. Sauer, N. Savinov, and A. Geiger, "Conditional affordance learning for driving in urban environments," in *Conference on Robot Learning (CoRL)*, 2018.

[68] M. Müller, A. Dosovitskiy, B. Ghanem, and V. Koltun, "Driving policy transfer via modularity and abstraction," in *Conference on Robot Learning (CoRL)*, 2018.

[69] N. Rhinehart, R. McAllister, and S. Levine, "Deep imitative models for flexible inference, planning, and control," arXiv:1810.06544, 2018.

[70] C. Hubschneider, A. Bauer, M. Weber, and J. M. Zollner, "Adding navigation to the equation: Turning decisions for end-to-end vehicle control," in *Intelligent Transportation Systems Conference (ITSC) Workshops*, 2017.

[71] F. Codevilla, M. Müller, A. M. López, V. Koltun, and A. Dosovitskiy, "End-to-end driving via conditional imitation learning," in *International Conference on Robotics and Automation (ICRA)*, 2018.

[72] Q. Wang, L. Chen, and W. Tian, "End-to-end driving simulation via angle branched network," arXiv:1805.07545, 2018.

[73] X. Liang, T. Wang, L. Yang, and E. Xing, "CIRL: Controllable imitative reinforcement learning for vision-based self-driving," in *European Conference on Computer Vision (ECCV)*, 2018.

[74] C. Innocenti, H. Lindén, G. Panahandeh, L. Svensson, and N. Mohammadiha, "Imitation learning for vision-based lane keeping assistance," in *Intelligent Transportation Systems Conference (ITSC)*, 2017.

[75] Z. Chen and X. Huang, "End-to-end learning for lane keeping of self-driving cars," in *Intelligent Vehicles Symposium (IV)*, 2017.

[76] H. M. Eraqi, M. N. Moustafa, and J. Honer, "End-to-end deep learning for steering autonomous vehicles considering temporal dependencies," in *Neural Information Processing Systems (NIPS)ML for ITS WS*, 2017.

[77] L. George, T. Buhet, E. Wirbel, G. Le-Gall, and X. Perrotton, "Imitation learning for end to end vehicle longitudinal control with forward camera," in *Neural Information Processing Systems (NIPS) Imitation Learning WS*, 2018.

[78] M. Bojarski, P. Yeres, A. Choromanska, K. Choromanski, B. Firner, L. Jackel, and U. Muller, "Explaining how a deep neural network trained with end-to-end learning steers a car," arXiv:1704.07911, 2017.

[79] J. Kim and J. Canny, "Interpretable learning for self-driving cars by visualizing causal attention," in *International Conference on Computer Vision (ICCV)*, 2017.

[80] Z. Li, T. Motoyoshi, K. Sasaki, T. Ogata, and S. Sugano, "Rethinking self-driving: Multi-task knowledge for better generalization and accident explanation ability," arXiv:1809.11100, 2018.

[81] C. Sun, A. Shrivastava, S. Singh, and A. Gupta, "Revisiting unreasonable effectiveness of data in deep learning era," in *International Conference on Computer Vision (ICCV)*, 2017.

[82] J. Hestness, S. Narang, N. Ardalani, G. Diamos, H. Jun, H. Kianinejad, M. M. A. Patwary, Y. Yang, and Y. Zhou, "Deep learning scaling is predictable, empirically," arXiv:1604.07316, 2017.

[83] A. Geiger, P. Lenz, and R. Urtasun, "Are we ready for autonomous driving? the KITTI vision benchmark suite," in *Int. Conf. on Computer Vision and Pattern Recognition (CVPR)*, 2012.

[84] M. Cordts, M. Omran, S. Ramos, T. Rehfeld, M. Enzweiler, R. Benenson, U. Franke, S. Roth, and B. Schiele, "The Cityscapes dataset for semantic urban scene understanding," in *Int. Conf. on Computer Vision and Pattern Recognition (CVPR)*, 2016.

[85] E. Santana and G. Hotz, "Learning a driving simulator," arXiv:1608.01230, 2016.

[86] W. Maddern, G. Pascoe, C. Linegar, and P. Newman, "1 Year, 1000 Km: The Oxford RobotCar dataset," *International Journal of Robotics Research (IJRR)*, vol. 36, no. 1, pp. 3–15, 2017.

[87] J. Kober, J. A. Bagnell, and J. Peters, "Reinforcement learning in robotics: A survey," *International Journal of Robotics Research (IJRR)*, vol. 32, no. 11, p. 12381274, 2013.

[88] V. Mnih, K. Kavukcuoglu, D. Silver, A. A. Rusu, J. Veness, M. G. Bellemare, A. Graves, M. Riedmiller, A. K. Fidjeland, G. Ostrovski, S. Petersen, C. Beattie, A. Sadik, I. Antonoglou, H. King, D. Kumaran, D. Wierstra, S. Legg, and D. Hassabis, "Human-level control through deep reinforcement learning," *Nature*, vol. 518, p. 529533, February 2015.

[89] P. Henderson, R. Islam, P. Bachman, J. Pineau, D. Precup, and D. Meger, "Deep reinforcement learning that matters," in *Conference on Artificial Intelligence (AAAI)*, 2018.

[90] N. D. Ratliff, J. A. Bagnell, and S. S. Srinivasa, "Imitation learning for locomotion and manipulation," in *International Conference on Humanoid Robots (HUMANOIDS)*, 2007.

[91] H. He, J. Eisner, and H. Daume, "Imitation learning by coaching," in *Neural Information Processing Systems (NIPS)*, 2012.

[92] A. survey of robot learning from demonstration, "Brenna D. argall and sonia chernova and manuela veloso and brett browning," *Robotics and Autonomous Systems*, vol. 57, no. 5, pp. 469–483, 2009.

[93] Z. Yang, Y. Zhang, J. Yu, J. Cai, and J. Luo, "End-to-end multi-modal multi-task vehicle control for self-driving cars with visual perceptions," in *International Conference on Pattern Recognition (ICPR)*, 2018.

[94] A. González, Z. Fang, Y. Socarras, J. Serrat, D. Vázquez, J. Xu, and A. M. López, "Pedestrian detection at day/night time with visible and fir cameras: A comparison," *Sensors*, vol. 16, no. 6, 2016.

[95] I. Sobh, L. Amin, S. Abdelkarim, K. Elmadawy, M. Saeed, O. A. Valeo, M. Gamal, and A. El-Sallab, "End-to-end multi-modal sensors fusion system for urban automated driving," in *Neural Information Processing Systems (NIPS) MLITS WS*, 2018.

[96] Q. Khan, T. Schön, and P. Wenzel, "Towards self-supervised high level sensor fusion," arXiv:1902.04272, 2019.

[97] D. Feng, C. Haase-Schutz, L. Rosenbaum, H. Hertlein, F. Duffhauss, C. Glaser, W. Wiesbeck, and K. Dietmayer, "Deep multi-modal object detection and semantic segmentation for autonomous driving: Datasets, methods, and challenges," arXiv:1902.07830, 2019.

[98] A. Dosovitskiy, G. Ros, F. Codevilla, A. López, and V. Koltun, "CARLA: An open urban driving simulator," in *Conference on Robot Learning (CoRL)*, 2017.

[99] K. Simonyan and A. Zisserman, "Very deep convolutional networks for large-scale image recognition," in *International Conference on Learning Representation (ICLR)*, 2015.

[100] E. Arnold, O. Y. Al-Jarrah, M. Dianati, S. Fallah, D. Oxtoby, and A. Mouzakitis, "A survey on 3d object detection methods for autonomous driving applications," *IEEE Trans. on Intelligent Transportation Systems*, January 2019.

[101] F. Codevilla, A. M. López, V. Koltun, and A. Dosovitskiy, "On offline evaluation of vision-based driving models," in *European Conference on Computer Vision (ECCV)*, 2018.

[102] B. Wymann, E. Espié, C. Guionneau, C. Dimitrakakis, R. Coulom, and A. Sumner, "TORCS, The Open Racing Car Simulator," <http://www.torcs.org>.

[103] C. Doersch and A. Zisserman, "Multi-task selfsupervised visual learning," in *International Conference on Computer Vision (ICCV)*, 2017.

[104] A. Kendall, Y. Gal, and R. Cipolla, "Multi-task learning using uncertainty to weigh losses for scene geometry and semantics," in *Int. Conf. on Computer Vision and Pattern Recognition (CVPR)*, 2018.

[105] S. haley Shwartz and A. Shashua, "On the sample complexity of end-to-end training vs. semantic abstraction training," arXiv:1604.06915, 2016.

[106] N. Kalra and S. M. Paddock, "Driving to safety: How many miles of driving would it take to demonstrate autonomous vehicle reliability?" *Transportation Research Part A: Policy and Practice*, vol. 94, p. 182193, December 2016.

[107] J. Zhang and K. Cho, "Query-efficient imitation learning for end-to-end simulated driving," in *Conference on Artificial Intelligence (AAAI)*, 2017.

[108] A. Amini, W. Schwarting, G. Rosman, B. Araki, S. Karaman, and D. Rus, "Variational autoencoder for end-to-end control of autonomous

driving with novelty detection and training de-biasing,” in *Int. Conf. on Intelligent Robots and Systems (IROS)*, 2018.

[109] C. Premebida, J. Carreira, J. Batista, and U. Nunes, “Pedestrian detection combining rgb and dense LiDAR,” in *Int. Conf. on Intelligent Robots and Systems (IROS)*, 2014.

[110] Y. Luo, J. Ren, M. Lin, J. Pang, W. Sun, H. Li, and L. Lin, “Single view stereo matching,” in *Int. Conf. on Computer Vision and Pattern Recognition (CVPR)*, 2018.

[111] D. Xu, W. Wang, H. Tang, H. Liu, N. Sebe, and E. Ricci, “Structured attention guided convolutional neural fields for monocular depth estimation,” in *Int. Conf. on Computer Vision and Pattern Recognition (CVPR)*, 2018.

APPENDIX
NETWORK ARCHITECTURES

In this Appendix we provide details on the CIL architectures used in this work. In all the tables we use the same terminology. M is the number of input perception channels. M=3 for RGB, M=1 for depth (D) only, M=4 for RGBD. As measurement input, only the current speed of the vehicle is used. The output are the steering angle, the throttle and the braking forces. There are four action branches. The speed branch is only used at training time for performing multi-task learning with the action branches. ReLU nonlinearities are applied after all hidden layers, and batch normalization is performed after convolutional layers. No dropout is applied after convolutional layers.

TABLE V
CIL NETWORK DETAILS (ORIGINAL AND EARLY FUSION).

| Module | Input Dimension | Output Channels | Num. of Kernels | Stride | Dropout |
|---------------|-----------------|-----------------|-----------------|--------|---------|
| Perception | 200 × 88 × M | 32 | 5 | 2 | 0.0 |
| | 98 × 48 × 32 | 32 | 3 | 1 | 0.0 |
| | 96 × 46 × 32 | 64 | 3 | 2 | 0.0 |
| | 47 × 22 × 64 | 64 | 3 | 1 | 0.0 |
| | 45 × 20 × 64 | 128 | 3 | 2 | 0.0 |
| | 22 × 9 × 128 | 128 | 3 | 1 | 0.0 |
| | 20 × 7 × 128 | 256 | 3 | 2 | 0.0 |
| | 9 × 3 × 256 | 256 | 3 | 1 | 0.0 |
| | 7 × 1 × 256 | 512 | - | - | 0.0 |
| | | 512 | - | - | 0.0 |
| Measurement | 1 | 128 | - | - | 0.0 |
| | 128 | 128 | - | - | 0.0 |
| Join | 512+128 | 512 | - | - | 0.3 |
| Action Branch | 512 | 256 | - | - | 0.5 |
| | 256 | 256 | - | - | 0.5 |
| | 256 | 3 | - | - | 0.0 |
| Speed Branch | 512 | 256 | - | - | 0.5 |
| | 256 | 256 | - | - | 0.5 |
| | 256 | 1 | - | - | 0.0 |

TABLE VI
MID FUSION NETWORK DETAILS

| Module | Input Dimension | Output Channels | Num. of Kernels | Stride | Dropout |
|--------------------|-----------------|-----------------|-----------------|--------|---------|
| Perception (RGB) | 200 × 88 × 3 | 32 | 5 | 2 | 0.0 |
| | 98 × 48 × 32 | 32 | 3 | 1 | 0.0 |
| | 96 × 46 × 32 | 64 | 3 | 2 | 0.0 |
| | 47 × 22 × 64 | 64 | 3 | 1 | 0.0 |
| | 45 × 20 × 64 | 128 | 3 | 2 | 0.0 |
| | 22 × 9 × 128 | 128 | 3 | 1 | 0.0 |
| | 20 × 7 × 128 | 256 | 3 | 2 | 0.0 |
| | 9 × 3 × 256 | 256 | 3 | 1 | 0.0 |
| | 7 × 1 × 256 | 512 | - | - | 0.0 |
| | 512 | 512 | - | - | 0.0 |
| Perception (Depth) | 200 × 88 × 1 | 32 | 5 | 2 | 0.0 |
| | 98 × 48 × 32 | 32 | 3 | 1 | 0.0 |
| | 96 × 46 × 32 | 64 | 3 | 2 | 0.0 |
| | 47 × 22 × 64 | 64 | 3 | 1 | 0.0 |
| | 45 × 20 × 64 | 128 | 3 | 2 | 0.0 |
| | 22 × 9 × 128 | 128 | 3 | 1 | 0.0 |
| | 20 × 7 × 128 | 256 | 3 | 2 | 0.0 |
| | 9 × 3 × 256 | 256 | 3 | 1 | 0.0 |
| | 7 × 1 × 256 | 512 | - | - | 0.0 |
| | 512 | 512 | - | - | 0.0 |
| Measurement | 1 | 128 | - | - | 0.0 |
| | 128 | 128 | - | - | 0.0 |
| Join | 512+512+128 | 512 | - | - | 0.3 |
| Action Branch | 512 | 256 | - | - | 0.5 |
| | 256 | 256 | - | - | 0.5 |
| | 256 | 3 | - | - | 0.0 |
| Speed Branch | 512 | 256 | - | - | 0.5 |
| | 256 | 256 | - | - | 0.5 |
| | 256 | 1 | - | - | 0.0 |

TABLE VII
LATE FUSION NETWORK DETAILS

| Module | Input Dimension | Output Channels | Num. of Kernels | Stride | Dropout |
|-----------------------|-----------------|-----------------|-----------------|--------|---------|
| Perception (RGB) | 200 × 88 × 3 | 32 | 5 | 2 | 0.0 |
| | 98 × 48 × 32 | 32 | 3 | 1 | 0.0 |
| | 96 × 46 × 32 | 64 | 3 | 2 | 0.0 |
| | 47 × 22 × 64 | 64 | 3 | 1 | 0.0 |
| | 45 × 20 × 64 | 128 | 3 | 2 | 0.0 |
| | 22 × 9 × 128 | 128 | 3 | 1 | 0.0 |
| | 20 × 7 × 128 | 256 | 3 | 2 | 0.0 |
| | 9 × 3 × 256 | 256 | 3 | 1 | 0.0 |
| | 7 × 1 × 256 | 512 | - | - | 0.0 |
| | 512 | 512 | - | - | 0.0 |
| Perception (Depth) | 200 × 88 × 1 | 32 | 5 | 2 | 0.0 |
| | 98 × 48 × 32 | 32 | 3 | 1 | 0.0 |
| | 96 × 46 × 32 | 64 | 3 | 2 | 0.0 |
| | 47 × 22 × 64 | 64 | 3 | 1 | 0.0 |
| | 45 × 20 × 64 | 128 | 3 | 2 | 0.0 |
| | 22 × 9 × 128 | 128 | 3 | 1 | 0.0 |
| | 20 × 7 × 128 | 256 | 3 | 2 | 0.0 |
| | 9 × 3 × 256 | 256 | 3 | 1 | 0.0 |
| | 7 × 1 × 256 | 512 | - | - | 0.0 |
| | 512 | 512 | - | - | 0.0 |
| Measurement (RGB) | 1 | 128 | - | - | 0.0 |
| | 128 | 128 | - | - | 0.0 |
| Measurement (Depth) | 1 | 128 | - | - | 0.0 |
| | 128 | 128 | - | - | 0.0 |
| Join (RGB) | 512+128 | 512 | - | - | 0.3 |
| Join (Depth) | 512+128 | 512 | - | - | 0.3 |
| Action Branch (RGB) | 512 | 256 | - | - | 0.5 |
| | 256 | 256 | - | - | 0.5 |
| | 256 | 3 | - | - | 0.0 |
| Action Branch (Depth) | 512 | 256 | - | - | 0.5 |
| | 256 | 256 | - | - | 0.5 |
| | 256 | 3 | - | - | 0.0 |
| Join (Streams) | 3+3 | 256 | - | - | 0.0 |
| Final Action | 256 | 128 | - | - | 0.0 |
| | 128 | 128 | - | - | 0.0 |
| | 128 | 3 | - | - | 0.0 |
| Speed Branch (RGB) | 512 | 256 | - | - | 0.5 |
| | 256 | 256 | - | - | 0.5 |
| | 256 | 1 | - | - | 0.0 |
| Speed Branch (Depth) | 512 | 256 | - | - | 0.5 |
| | 256 | 256 | - | - | 0.5 |
| | 256 | 1 | - | - | 0.0 |
| Join (Speeds) | 1+1 | 256 | - | - | 0.0 |
| Final Speed | 256 | 128 | - | - | 0.0 |
| | 128 | 128 | - | - | 0.0 |
| | 128 | 1 | - | - | 0.0 |